

Collision probability of tethers and sails against debris

Ricardo García-Pelayo*

ETS Ingeniería Aeronáutica, UPM, Madrid 28040, Spain

Juan Luis Gonzalo†

Politecnico di Milano, Italy

Claudio Bombardelli ‡

ETS Ingeniería Aeronáutica, UPM, Madrid 28040, Spain

Abstract

The work done on probability of collision between spherical objects in orbit is extended here to the case of one spherical object and one circular or rectangular object. The former is a model for spacecraft or debris, while the latter is a model for a sail or a tether. Two kinds of computations are done. The first kind is the computation of the collision rate when the flux of one object (typically debris) with respect to the other object is known. This information is important when planning a mission. The second kind is the computation of the collision probability for a particular pair of objects whose probability density functions of the positions are known. This information is necessary to decide if an evasive maneuver is going to be performed or not.

1 Introduction

Estimating the rate or probability of collision between orbiting objects is a fundamental task in space security awareness. The rate is required, for instance, in order to assess the chance of a satellite experiencing one or more collisions in its lifetime as it interacts with the surrounding debris environment. The probability of collision needs to be computed whenever an active spacecraft experiences a critical conjunction in order to determine whether or not a propulsive collision avoidance maneuver should be performed. Lastly, if a maneuver is eventually required it can only be optimized with the aid of a proper collision probability estimation method [1].

There is an abundant literature dealing with the computation of the collision probability when the two approaching bodies are spheres [2, 3, 4, 5, 6, 7]. Of these, the methods

*E-mail: r.garciapelayo@upm.es

†E-mail: juanluis.gonzalo@polimi.it

‡E-mail: claudio.bombardelli@upm.es

[6, 7] are the most computationally efficient. Method [7] is the only one that can be applied to the non-Gaussian case.

The spherical envelope of the true spacecraft geometry provides a good conservative bound of the collision probability for the case of, say, two satellites. But it becomes overly simplistic when at least one of the two objects is far from spherical. Large circular or rectangular solar sails of tens to hundreds of square meters surface and km-long tethers, for instance, are envisioned as passive deorbiting devices to be deployed at the end-of-life of future spacecraft to provide a low-cost reentry in low earth orbit (LEO). Actually the European Space Agency is interested in the computation of the rate and probability of collision that we mentioned in the first paragraph. This is part of the study in which the authors have been involved and which has motivated them to write the present paper.

The need to compute collision probabilities and rates of non spherical objects has been recognized before. An outline of how to decompose the International Space Station into rectangular pieces to compute its probability of collision is given in Chapter 6 of [4]. More recently a computation of the collision probability for rectangular cross section was presented [8], but it used some approximations that we do without in the present article.

There is a software [9] which can be used to compute the rate of collision of orbiting ellipsoids, and an ellipsoid can be a sphere and can be made to approach a tether. But this approach works with pairs of satellites and requires a catalog, whereas our approach is analytical and we work with a satellite and a flux obtained from a database (for example ORDEM [10] or MASTER [11]).

The attitude of a dead satellite is a complicated matter, but taking its attitude to be random is a reasonable assumption ([12], p. 13). Taking the maximum projected area on the collision plane seems to be a conservative assumption, and this has been done for cuboids [13], [14] and therefore for rectangles as a particular case. But if an upper bound of the actual projection area is used, the deorbiting time is underestimated, therefore it is not clear if taking the maximum projected area is actually a safer option than taking the attitude to be random.

The goal of this article is to provide formulae for the collision rate and the collision probability of tethers and rectangular or circular sails (henceforth, body MM) against satellites or debris, modeled by spheres (henceforth, body SS). All of the results are analytical except for the calculation of the collision probability of a rectangle and a sphere, for which a very efficient program has been written.

In section 2 the general theoretical setup of this article is laid down. In section 3 we are interested in the rate of collision of body MM with *any* satellite or debris over a long interval of time. A typical use of this rate is to estimate the survival probability of a certain mission. In subsection 3.1 the projection M of MM onto the encounter plane stays the same over the long interval of time. In subsection 3.2 MM tumbles around randomly. In section 4 the probability of collision of body MM against one particular body SS is found. We suppose that the conditions of short-encounter model [2, 15, 3, 5, 4, 16, 1, 6] are fulfilled and that the probability density functions (henceforth, pdf) of the positions of both body MM and body SS are known. A typical use of this probability of collision is to decide if an evasive maneuver is going to be made or not. In section 5 the advantages of our formulae over the sphere approximation and some numerical results are discussed.

2 Probability of collision during a short encounter

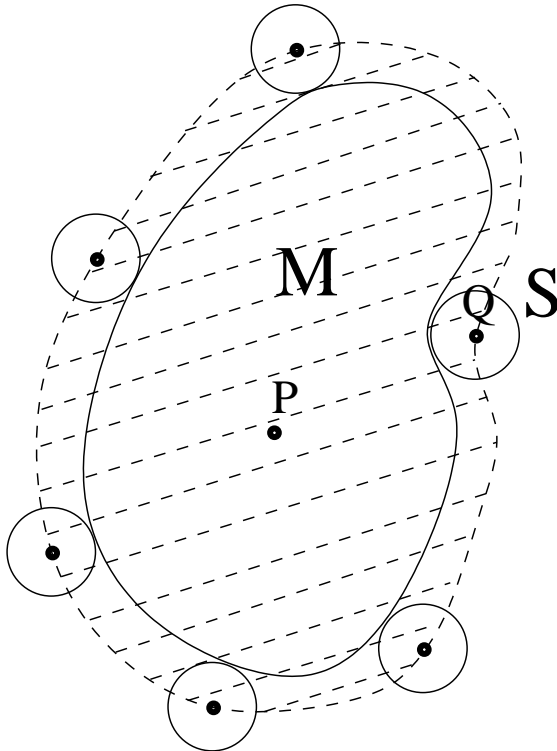


Figure 1: The collision region in the encounter plane is found by sliding the projection of the debris or the satellite (the circle S) around the projection M .

Whether we want to find collision rate or the collision probability, the first step is to find the region of collision in the encounter plane, which is the plane perpendicular to the relative velocity \vec{v} of bodies MM and SS . Let M and S denote the projections of bodies MM and SS onto the encounter plane (also known as b -plane). Then, as shown in Fig. 1, the collision region is the shaded region, which is obtained by sliding S (the projection of the debris or the satellite) around M . When the S comes back to its original position, the point Q shown in Fig. 1 has drawn the contour of the shaded region. We shall denote the shaded region by $M \oplus (-S)$, because it is the Minkowski sum of the projections of M and the inversion of S ([17], remark at the end of p. 12). For a proof see Appendix 1.

For a more complicated example of Minkowski sum of two projections of spacecraft, see Fig. 11 of [18]. For a more detailed exposition of the relation between the collision region and the Minkowski sum see Appendix 1.

Let ρ be the pdf of the vector \overrightarrow{PQ} (see Fig. 1). Then the probability of collision between MM and SS is

$$\int_{M \oplus (-S)} d^2r \rho(\vec{r}). \quad (1)$$

In order to find the collision probability we need both the dashed region Ms and ρ . But to find the rate the latter will suffice.

We now show how to find the projection ρ of the pdf of the relative position \overrightarrow{PQ} onto the encounter plane.

We assume that pdf's of the positions P and Q , ρ_P and ρ_Q , respectively, are given. That is, $\rho_P(\vec{r}) d^3r$ is the probability that the point P is in the interval $[x, x + dx] \times [y, y + dy] \times [z, z + dz]$, and a similar statement defines ρ_Q . Then, since ρ_P and ρ_Q are independent, the probability density that \overrightarrow{PQ} be equal to \vec{r} is the integral over all possible ways in which the positions of P and Q differ by a vector \vec{r} , that is,

$$\rho_{rel}(\vec{r}) = \int d^3r' \rho_P(\vec{r}') \rho_Q(\vec{r} + \vec{r}') = \int d^3r' \rho_P(-\vec{r} + \vec{r}') \rho_Q(\vec{r}'). \quad (2)$$

Note that if ρ_P and ρ_Q are Gaussians, then ρ_{rel} is also a Gaussian.

ρ is the projection of ρ_{rel} onto the encounter plane, that is for any \vec{r} in the encounter plane,

$$\rho(\vec{r}) = \int d\lambda \rho_{rel}(\vec{r} + \lambda\vec{v}), \quad (3)$$

where \vec{v} is the relative velocity. Note that ρ is a marginal distribution.

3 Rate of collision over a long interval of time

In the present section we provide a general scheme to assess the collision probability of a non-spherical body MM with a population of spherical debris over an interval of time which includes many orbital periods.

Strictly speaking, collisions are correlated random events. For example, debris originated in an explosion appears in clouds [19], so that if a collision with a piece of debris in the cloud has taken place, then for a short period of time the satellite is likely to still be in that cloud and has a larger than usual probability of colliding again. Debris of astronomical origin which is in solar orbit also comes in clouds. However, collisions are very unlikely, and the mean time between collisions is much larger than the time that the satellite spends in a cloud. Therefore, over long intervals of time, collisions are uncorrelated random events. Therefore their occurrence is a Poisson process [20] whose rate we want to determine. It follows from (1) that, on the average, the probability that the result of flyby is a collision is

$$\bar{\rho} A(M \oplus (-S)), \quad (4)$$

where $A(M \oplus (-S))$ is the area of the Minkowski sum and $\bar{\rho}$ is the average value of ρ . In a flyby $\bar{\rho}$ is the inverse of the area of the region of the encounter plane where the incoming debris might be found. The rate of collision of the Poisson process is $\bar{\rho}A(M \oplus (-S))$ divided by the time Δt between flybys. We now determine this rate.

For each incoming sphere SS there is a different encounter plane which yields a different Minkowski sum $M \oplus (-S)$. We are going to derive first the case in which all of the incoming spheres have the same size and direction. Let ϕ be their flux in the MM

system of reference. For example this flux can be obtained from the ORDEM [10] or MASTER [11] databases, where it is given in the system of reference of an object MM whose orbital parameters are given by the user. These spheres SS are normally incident on $M \oplus S$. $\bar{\rho}$ is a surface density of spheres SS , because it has dimensions of L^{-2} (inverse length squared). The number of spheres SS incident on $M \oplus (-S)$ during a time Δt is, by definition of flux, equal to $\phi A(M \oplus (-S))\Delta t$. The surface density of spheres on $M \oplus (-S)$ is then $\phi\Delta t = \bar{\rho}$ and the Poisson rate wanted in the last sentence of the last paragraph is $\phi A(M \oplus (-S))$. The probability of n collisions during an interval t is

$$e^{-\phi A(M \oplus (-S))t} \frac{(\phi A(M \oplus (-S)))^n}{n!}. \quad (5)$$

The most interesting case is $n = 0$, which yields the survival probability, $e^{-\phi A(M \oplus (-S))t}$.

Note that eq. (5) is a generalization of formula (3.2) in [21]. Indeed, formula (3.2) in [21] is formula (5) with $A(M \oplus (-S))$ substituted by $A(M)$. When the size of the debris is small compared to the size of MM , formula (3.2) in [21] may be used. When SS is large debris or satellites, their size must be included in the analysis and expression (5) must be used.

So far we have obtained the collision rate for fixed size and incoming direction of the spheres SS . For an arbitrary distribution of sizes and incoming directions one has to weigh by the distribution and integrate over the sizes of the spheres and the directions of the flux.

3.1 Fixed attitude with respect to the encounter plane

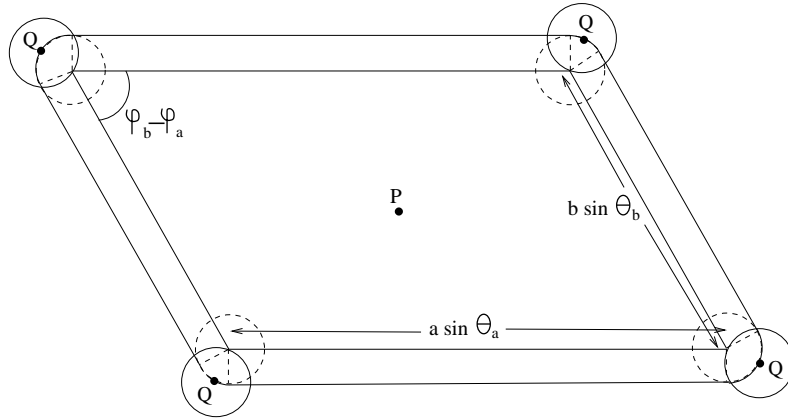


Figure 2: Minkowski sum of a rectangle and a sphere.

Most of the time, collision is with small debris. Then the rim in Fig. 1 is negligible and $A(M \oplus (-S))$ may be very well approximated by $A(M)$. However, tethers and sails may also collide with active or dead spacecraft, whose sizes are not negligible compared to the size of the sail or tether. Then the area of the rim in Fig. 1 (that is, the region between M and $M \oplus (-S)$) has to be taken into account. When the projection M is a parallelogram and the radius of the sphere is R , it is clear from Fig. 2 that the area

of $M \oplus (-S)$ is the projected area of the rectangle + (the projected perimeter of the rectangle $\times R$) + πR^2 , that is

$$A(M \oplus (-S)) = A(M) + \text{per}(M)R + \pi R^2, \quad (6)$$

where $\text{per}(M)$ is the perimeter of M . This formula holds whenever the projection M is convex. Indeed, the Steiner-Minkowski theorem gives a formula for the computation of the n -dimensional volume of Minkowski sums of convex bodies and spheres. When $n = 2$ this formula is simply the above formula ([22], p. 116).

In this section we are going to find the area $A(M \oplus (-S))$ to be substituted in formula (5) for a rectangular sail, a tether and a circular sail.

3.1.1 Rectangle

The projection of a rectangle onto a plane is a parallelogram. Indeed, a projection is a linear transformation (see, e. g., [23], p. 113). Therefore, it transforms parallel lines into parallel lines.

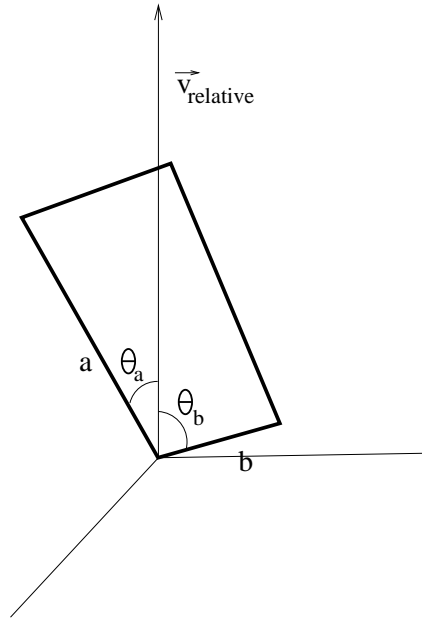


Figure 3: Angles θ_a and θ_b are shown.

Fig. 2 is useful to follow parts of this paragraph. Let θ_a and θ_b be the angles made by the direction of the relative velocity and the directions of the sides of the rectangular sail (see Fig. 3). We define a Cartesian coordinate frame whose z -axis is parallel to \vec{v} . Then we define spherical coordinates where θ is the colatitude (angle made with the positive direction of the z -axis) and φ is the longitude. The coordinates of the unit vectors associated with the sides of the sail are $\vec{u}_a = (\sin \theta_a \cos \varphi_a, \sin \theta_a \sin \varphi_a, \cos \theta_a)$ and $\vec{u}_b = (\sin \theta_b \cos \varphi_b, \sin \theta_b \sin \varphi_b, \cos \theta_b)$. The cosine of the angle θ_M made by the z -axis and the vector perpendicular to the sail is the third component of $\vec{u}_a \times \vec{u}_b$, which is

$$\cos \theta_M = \sin(\varphi_b - \varphi_a) \sin \theta_a \sin \theta_b. \quad (7)$$

Since \vec{u}_a and \vec{u}_b are perpendicular, $\vec{u}_a \cdot \vec{u}_b = \cos \theta_a \cos \theta_b + \sin \theta_a \sin \theta_b \cos(\varphi_b - \varphi_a) = 0 \Rightarrow$

$$\cos(\varphi_b - \varphi_a) = -\frac{\cos \theta_a \cos \theta_b}{\sin \theta_a \sin \theta_b}. \quad (8)$$

Therefore,

$$A(M) = ab \cos \theta_M = ab \sqrt{1 - \left(\frac{\cos \theta_a \cos \theta_b}{\sin \theta_a \sin \theta_b} \right)^2} \sin \theta_a \sin \theta_b = ab \sqrt{-\cos(\theta_a + \theta_b) \cos(\theta_a - \theta_b)} \quad (9)$$

and

$$A(M \oplus (-S)) = ab \sqrt{-\cos(\theta_a + \theta_b) \cos(\theta_a - \theta_b)} + 2(a \sin \theta_a + b \sin \theta_b)R + \pi R^2. \quad (10)$$

This is the expression to be substituted in equation (5).

Of course $M \oplus (-S)$ in Fig. 2 could have been circumscribed by a larger parallelogram, but the formula for its area is not simpler than the preceding exact formula.

3.1.2 Tether



Figure 4: Minkowski sum of a rectangle and a disk. Only the two large contributions at the sides are kept in expression (11).

We have seen that the projection of a rectangle is not a rectangle but (in general) a parallelogram. Likewise, the projection of a cylindrical or tape tether onto a plane is not a rectangle. However, the difference between its projection and a rectangle is very small. This is because the length to width ratio of tethers is of the order of 10^5 . Furthermore, a subsatellite of non negligible size and mass is in most of the cases attached to the tether end for various purposes. For instance in a mechanical tether it can be a ballast mass to

ease the tether deployment, while in an electrodynamic tether the subsatellite may host an electron emitting device (e.g. a hollow cathode) to maximize the transmitted current. Therefore we may forget about the non-rectangular part of the projection altogether.

We denote α to be the angle made by the tether and the collision plane.

Case 1) Round tether of radius r and length L . Its projection on the collision plane is a rectangle of width $2r$ and length $L \cos \alpha$. According to the formula (6), $A(M \oplus S) = 2rL \cos \alpha + 2R(2r + L \cos \alpha) + \pi R^2$. However, as explained at the beginning of this subsection, we neglect the contributions of the ends of the tether, because that part of the Minkowski sum is going to be taken into account by the Minkowski sum of the satellite or the hollow cathode and the sphere. Therefore we just keep the contribution (see Fig. 4)

$$2rL \cos \alpha + 2RL \cos \alpha = 2(R + r)L \cos \alpha. \quad (11)$$

If the sphere is not small debris but a satellite, the above expression may be approximated by $2RL \cos \alpha$.

Case 2) The tether is a tape of length L , width w (a typical value for w would be 2 cm) and negligible thickness. The edges of the tape are not straight; the tape is twisted and its projection on a plane has sinusoidal edges, as shown in Fig. 5. While a computation of the Minkowski sum is in principle possible, one may also substitute the actual projection by a rectangle with the same axis of symmetry and width $2w/\pi$, which has the same area as the actual projection (see Fig. 5). Indeed, let β be the angle made by some straight line and some segment. We compute the average of the projection of the segment over the straight line over the range $[0, \pi/2]$, which, by symmetry, is the same as the average over the range $[0, 2\pi]$. The probability density function of the uniform density in the range $[0, \pi/2]$ is the constant $\frac{1}{\pi/2}$. Therefore the factor by which the length of the segment has to be multiplied is $\int_0^{\pi/2} d\beta \frac{\cos \beta}{\pi/2} = \frac{2}{\pi}$. Thus if w is the width of the tape, $2w/\pi$ is its twisted width. With this approximation, the projection on the collision plane is a rectangle of width $2w/\pi$ and length $L \cos \alpha$. According to formula (6), the area of the Minkowski sum is $((2w/\pi)L \cos \alpha + 2R((2w/\pi) + L \cos \alpha)) + \pi R^2$. For the same reasons that lead to expression (11), we just keep the contribution

$$\frac{2w}{\pi}L \cos \alpha + 2RL \cos \alpha = 2\left(\frac{w}{\pi} + R\right)L \cos \alpha. \quad (12)$$

If the sphere is not small debris but a satellite, the above expression may be approximated by $2RL \cos \alpha$.

3.1.3 Disk

First we show that the projection of a disk of radius a onto a plane pl is an ellipse. Let θ_M be the angle between pl and the plane which contains the disk. Construct a Cartesian coordinate frame whose x -axis is the intersection between the plane which contains the disk and the plane pl , whose z -axis is perpendicular to the plane pl and whose y -axis is perpendicular to the other two and completes a right-handed frame. Then the projection of the diameter of the disk which is parallel to the x -axis still has radius a , but all chords perpendicular to the said diameter shrink by a factor $\cos \theta_M$ when projected. An ellipse

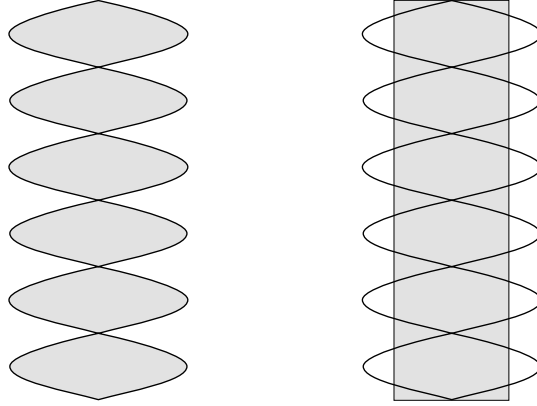


Figure 5: To the left, projection of a twisted tape on to a plane. To the right, projection of a twisted tape on to a plane and a rectangle of the same area.

of semiaxes a and b can be obtained from a disk of radius a by a dilation, as is clear from the Cartesian formula $(x/a)^2 + (y/b)^2 = 1$. Therefore the said projection is indeed an ellipse of semiaxes a and $a \cos \theta_M$.

The perimeter of an ellipse of semiaxes a and b is $4aE\left(1 - \frac{b^2}{a^2}\right)$, where E is the complete elliptic integral of the second kind. It follows that

$$A(M \oplus (-S)) = \pi R_{sail}^2 \cos \theta_M + 4R_{sail}E(\sin^2 \theta_M)R + \pi R^2, \quad (13)$$

where R_{sail} is the radius of the disk. This is the expression to be substituted in equation (5).

3.2 Random attitude

If we take the attitude of body MM to be random, then we need to compute the average area of $M \oplus S$ when the attitude of body MM is averaged over. Fortunately, as we shall see, there is a simple formula when MM is a flat, convex surface.

Lemma. Let ℓ be the length of a flat curve Γ (i. e., $\int_{\Gamma} dr = \ell$) contained in a plane whose normal makes an angle θ with the z -axis. Then the average (with respect to rotations of the curve Γ in its plane) of the length of the projection of the curve Γ onto the xy -plane is

$$\frac{2}{\pi}E(\sin^2 \theta)\ell, \quad (14)$$

where E is the complete elliptic integral of the second kind.

Proof. Let x' and y' be Cartesian coordinates for the plane in which the curve Γ lies. We may, without loss of generality, suppose that the axis x' and the axis x are the same, so that the normal to the plane containing the curve Γ is contained in the yz -plane. Consider an oriented element of length $d\vec{r}'$ of the curve Γ which makes an angle φ' with the x' -axis, that is, $d\vec{r}' = |d\vec{r}'|(\cos \varphi', \sin \varphi', 0)$. In x, y, z coordinates the unit vector $(\cos \varphi', \sin \varphi', 0)$ is

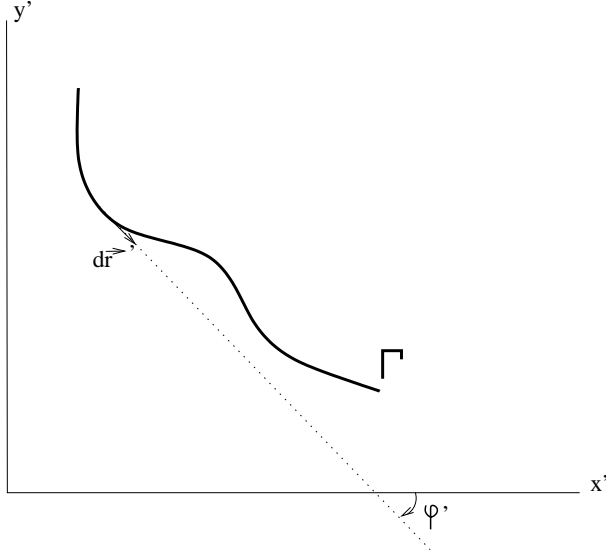


Figure 6: Curve Γ to be projected onto the xy plane.

$$\begin{pmatrix} 1 & 0 & 0 \\ 0 & \cos \theta & \sin \theta \\ 0 & -\sin \theta & \cos \theta \end{pmatrix} \begin{pmatrix} \cos \varphi' \\ \sin \varphi' \\ 0 \end{pmatrix} = \begin{pmatrix} \cos \varphi' \\ \sin \varphi' \cos \theta \\ -\sin \varphi' \sin \theta \end{pmatrix}, \quad (15)$$

the length of whose projection on the xy -plane is $\sqrt{\cos^2 \varphi' + \sin^2 \varphi' \cos^2 \theta}$. The average of this expression over the angle φ' is

$$\frac{2}{\pi} \int_0^{\pi/2} d\varphi' \sqrt{\cos^2 \varphi' + \sin^2 \varphi' \cos^2 \theta} = \frac{2}{\pi} E(\sin^2 \theta). \quad (16)$$

Therefore the average projected length is

$$\frac{2}{\pi} \int_0^{\pi/2} d\varphi' \int_{\Gamma} dr \sqrt{\cos^2 \varphi' + \sin^2 \varphi' \cos^2 \theta} = \int_{\Gamma} dr \frac{2}{\pi} E(\sin^2 \theta) = \frac{2}{\pi} E(\sin^2 \theta) \ell. \quad \text{QED.} \quad (17)$$

Note that the above lemma is true regardless of whether the curve Γ is open or closed, convex or concave. The formula for the length of an ellipse, $4aE\left(1 - \frac{b^2}{a^2}\right)$, is a particular case of the above formula, since an ellipse of semiaxes a and b is the projection on the xy -plane of a circle which makes an angle $\arccos(b/a)$ with the said plane.

The projected surface of a flat figure of area A contained in a plane whose normal makes an angle θ with the z -axis is $A \cos \theta$. The element of surface in spherical coordinates is $r^2 \sin \theta d\theta dr$. Therefore, the probability that the colatitude be θ is proportional to $\sin \theta$. Since $\int_0^{\pi/2} d\theta \sin \theta = 1$, the Steiner-Minkowski formula (6) yields that the average collision cross section when the orientation of a convex flat figure is isotropic is

$$\int_0^{\pi/2} d\theta \sin \theta \left(A \cos \theta + \frac{2}{\pi} E(\sin^2 \theta) \ell R + \pi R^2 \right) = \frac{A}{2} + \frac{\pi \ell R}{4} + \pi R^2. \quad (18)$$

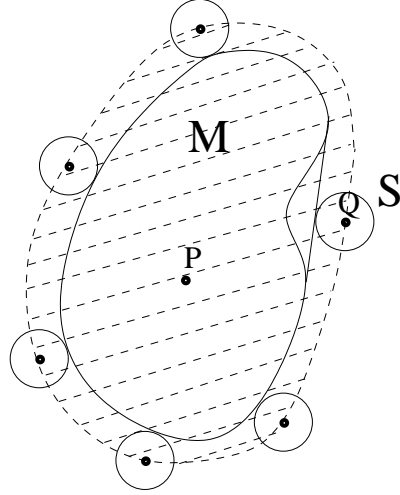


Figure 7: It is seen in this example that $M \oplus S \subset M_{env} \oplus S$, as proven in the text.

Example 1. The figure is a **rectangle** of sides a and b . Its average collision cross section is

$$\overline{A(M \oplus (-S))} = \frac{ab}{2} + \frac{\pi(a+b)R}{2} + \pi R^2. \quad (19)$$

Example 2. The figure is a **disk** of radius R_{sail} . Its average collision cross section is

$$\overline{A(M \oplus (-S))} = \frac{\pi R_{sail}^2}{2} + \frac{\pi^2 R_{sail} R}{2} + \pi R^2. \quad (20)$$

For the reasons given in subsection 2.1.2, the case of the tether ($b \ll a$) would be $\frac{ab}{2} + \frac{\pi a R}{2}$, with b the width of the cylindrical tether, or $b = 2/\pi$ times its width if it is a tape. However, the attitude of the tether is not random, because of the large disparity between its moments of inertia and the gravity gradient [24].

The convex envelope of a body is the smallest convex body which contains it. When this body is a flat figure, the convex envelope is the figure made by a rubber band which surrounds the figure. It is intuitive that, as depicted in Fig. 7, $M \oplus (-S) \subset M_{env} \oplus (-S)$. Indeed, $M \subset M_{env} \Rightarrow M_{env} = M \cup M'$, where $M' = M_{env} - M$. The Minkowski sum is distributive with respect to the union of sets (see Appendix 1), therefore $M_{env} \oplus (-S) = (M \oplus (-S)) \cup (M' \oplus (-S)) \supset M \oplus (-S)$.

We use this result to bound the average collision cross section of a **concave** flat figure:

$$\overline{A(M \oplus (-S))} \leq \frac{A_{env}}{2} + \frac{\pi \ell_{env} R}{4} + \pi R^2, \quad (21)$$

where A_{env} and ℓ_{env} are the area and the perimeter of the convex envelope, respectively.

4 Probability of collision for rectangles, tethers and disks

We are going to suppose that ρ_{rel} is a Gaussian, because the pdf's of the position, in terms of which ρ_{rel} is defined, are almost always given as Gaussians. Then the integral in (1) cannot be done for arbitrary Minkowski sum. In particular, it cannot be done for the Minkowski sum of a circle and an ellipse or the Minkowski sum of a circle and a parallelogram. However, the Minkowski sum of a circle and an ellipse, and the Minkowski sum of a circle and a parallelogram can be tightly enclosed by an ellipse and by a parallelogram, respectively. Good analytical approximations for the computation of the integral in (1) are available when Ms is the ellipse or the parallelogram, as we shall see.

4.1 The rectangle

An upper bound for the probability of collision is

$$\int_{Par(M \oplus (-S))} \rho(\vec{r}), \quad (22)$$

where $Par(M \oplus (-S))$ is the enclosing parallelogram shown in Fig. 8 of the Minkowski sum shown in Fig. 2. If R is the radius of the sphere, the sides of the enclosing parallelogram are at a distance R from the projection of the rectangle. We need to find the length added to each of the sides shown in Figure 8. In the left figure the two kinds of kites whose sides we need to find are shown in dashed lines. The angles made by the sides of the kites which join at the vertex of the parallelogram are $\varphi_b - \varphi_a$ for the right upper kite and $\pi - (\varphi_b - \varphi_a)$ for the right lower kite. In the right figure, the angle made by the two segments of length R is $\pi - (\varphi_b - \varphi_a)$. It is easy to see that the length of the dotted segment is $2R \sin((\pi - (\varphi_b - \varphi_a))/2) = 2R \cos((\varphi_b - \varphi_a)/2)$. The larger triangle is an isosceles triangle whose angles have values $(\pi - (\varphi_b - \varphi_a))/2$ and $\varphi_b - \varphi_a$. It follows from the sine theorem that $x = 2R \cos^2((\varphi_b - \varphi_a)/2) / \sin(\varphi_b - \varphi_a) = R \tan \frac{\pi - (\varphi_b - \varphi_a)}{2}$. Likewise, for the right upper kite the added length is $x = 2R \sin^2((\varphi_b - \varphi_a)/2) / \sin(\varphi_b - \varphi_a) = R \tan \frac{\varphi_b - \varphi_a}{2}$. Then the length added to each of the sides is

$$R \tan \frac{\pi - (\varphi_b - \varphi_a)}{2} + R \tan \frac{\varphi_b - \varphi_a}{2} = \frac{2R}{\sin(\varphi_b - \varphi_a)} = \frac{R \sin(\theta_a + \theta_b)}{\sqrt{-\cos(\theta_a + \theta_b) \cos(\theta_a - \theta_b)}}, \quad (23)$$

where the last equality can be obtained from eqs. (8) and (9).

The enclosing parallelogram is now completely determined. The problem at hand is to evaluate the integral

$$\frac{1}{2\pi\sigma_x\sigma_y} \int_{Par(M \oplus (-S))} d^2r \exp -\frac{1}{2} \left(\frac{x^2}{\sigma_x^2} + \frac{y^2}{\sigma_y^2} \right), \quad (24)$$

which is a tight upper bound for the collision probability. In order to do this integral we shall develop a method for the computation of bivariate normal probabilities in rectangular domains based on the work of Genz [25].

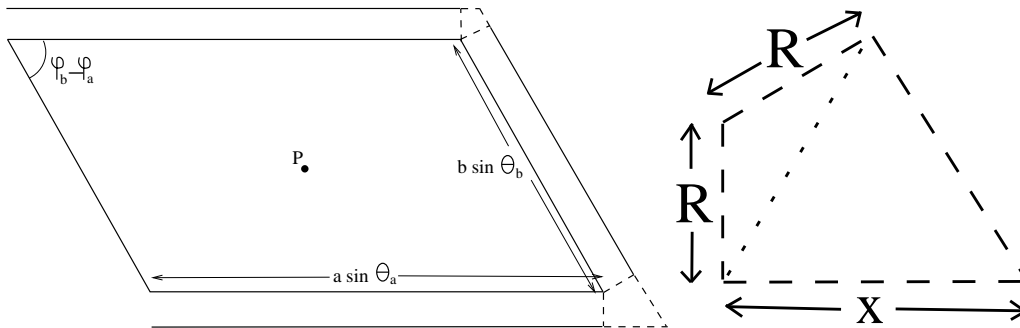


Figure 8: In the left figure the two kinds of kites whose sides we need to find are shown in dashed lines. In the right figure one of them is amplified.

In [25] Genz proposes and compares several algorithms for the numerical computation of bivariate, trivariate normal distribution and Student t probability distributions. In particular, a very fast algorithm is presented for computing the bivariate normal probability $L(h, k, \rho)$ for a domain of the form $[h, \infty) \times [k, \infty)$ ($h, k \in \Re$) and a Gaussian of correlation $\rho \in [0, 1]$ and $\sigma_x = \sigma_y = 1$. Note that L is related to the standard bivariate normal cumulative distribution Φ by the expression $\Phi((x, y), \rho) = L(-x, -y, \rho)$. A more detailed description of the algorithm can be found in Appendix 4.

To apply this algorithm, the domain and the covariance matrix have to be transformed so that the former becomes a rectangle and the latter a correlation matrix. Let $V_0 = (x_0, y_0)$ be a vertex of the parallelogram, and let $(x_1, y_1), (x_2, y_2)$ be the coordinates of the two vertices adjacent to V_0 . We define

$$\vec{a} = (a_x, a_y) \equiv (x_1, y_1) - (x_0, y_0) \quad \text{and} \quad \vec{b} = (b_x, b_y) \equiv (x_2, y_2) - (x_0, y_0), \quad (25)$$

where \vec{a} and \vec{b} are the vectors representing the sides of the parallelogram departing from V_0 . It is then possible to find a linear transformation, defined by matrix M , that transforms the parallelogram into a square of unit side by imposing:

$$M\vec{a} = \begin{pmatrix} 1 \\ 0 \end{pmatrix}, \quad M\vec{b} = \begin{pmatrix} 0 \\ 1 \end{pmatrix}. \quad (26)$$

Combining these two equations and solving for M yields:

$$M \equiv \begin{pmatrix} a_x & b_x \\ a_y & b_y \end{pmatrix}^{-1} \quad (27)$$

Note that the resulting linear transformation will exist as long the matrix formed by \vec{a} and \vec{b} is invertible, that is, if both vectors are linearly independent. This condition will be met by any non-degenerate parallelogram.

The new domain is a square of unit side, defined by vertex

$$V_0^* = \begin{pmatrix} x_0^* \\ y_0^* \end{pmatrix} \equiv MV_0, \quad (28)$$

and side vectors $\vec{a}^* = (a_x^*, a_y^*) \equiv (1, 0)$ and $\vec{b}^* = (b_x^*, b_y^*) \equiv (0, 1)$. The covariance matrix will transform to:

$$\begin{pmatrix} \sigma_x^{*2} & \sigma_{xy}^* \\ \sigma_{xy}^* & \sigma_y^{*2} \end{pmatrix} \equiv M \begin{pmatrix} \sigma_x^2 & 0 \\ 0 & \sigma_y^2 \end{pmatrix} M^T, \quad (29)$$

which is in general not diagonal.

In the algorithm by Genz a correlation matrix instead of a covariance matrix is used, so one final transformation is needed. By applying two dilations (or contractions) of magnitudes $1/\sigma_x^*$ and $1/\sigma_y^*$ along the x and y axes, respectively, the covariance matrix becomes a correlation matrix:

$$\begin{pmatrix} 1 & \rho' \\ \rho' & 1 \end{pmatrix} \equiv \begin{pmatrix} 1 & \sigma_{xy}^*/\sigma_x^*\sigma_y^* \\ \sigma_{xy}^*/\sigma_x^*\sigma_y^* & 1 \end{pmatrix}, \quad (30)$$

and the domain becomes a rectangle of vertex

$$V'_0 = \begin{pmatrix} x'_0 \\ y'_0 \end{pmatrix} \equiv \begin{pmatrix} x_0^*/\sigma_x^* \\ y_0^*/\sigma_y^* \end{pmatrix}, \quad (31)$$

and side vectors $\vec{a}' = (a'_x, a'_y) \equiv (1/\sigma_x^*, 0)$ and $\vec{b}' = (b'_x, b'_y) \equiv (0, 1/\sigma_y^*)$.

Calling *Rect* the new domain, it is possible to write

$$\begin{aligned} & \frac{1}{2\pi\sigma_x\sigma_y} \int_{Par(Ms)} d^2r \exp -\frac{1}{2} \left(\frac{x^2}{\sigma_x^2} + \frac{y^2}{\sigma_y^2} \right) = \\ & \frac{1}{2\pi\sqrt{1-\rho'^2}} \int_{Rect} d^2r \exp \frac{-(x^2 - 2\rho'xy - y^2)}{2(1-\rho'^2)} = \Phi(Rect, \rho'), \end{aligned} \quad (32)$$

where the latter can be computed numerically by combining four calls to the bivariate normal probability function considered by Genz:

$$\Phi(Rect, \rho') = L(x'_0, y'_0, \rho') - L(x'_0 + a'_x, y'_0, \rho') - L(x'_0, y'_0 + b'_y, \rho') + L(x'_0 + a'_x, y'_0 + b'_y, \rho'). \quad (33)$$

We have programmed a web app implementing $\Phi(Rect, \rho')$ in JavaScript, which can be found at

<http://sdg.aero.upm.es/index.php/online-apps/gaussian-over-parallelogram>.

4.2 The very thin rectangle (tether)

If the body MM is a tether then we can approximate its projection on the encounter plane by a rectangle, as argued in subsection 2.1.2.

The probability caught by a rectangle of axes parallel to the principal axes of a Gaussian is

$$\begin{aligned} & \int_{x_1}^{x_2} dx \frac{e^{-\frac{1}{2}\frac{x^2}{\sigma_x^2}}}{\sqrt{2\pi\sigma_x^2}} \int_{y_1}^{y_2} dy \frac{e^{-\frac{1}{2}\frac{y^2}{\sigma_y^2}}}{\sqrt{2\pi\sigma_y^2}} = \\ & \frac{1}{2} \left(\operatorname{erf}\left(\frac{x_2}{\sqrt{2}\sigma_x}\right) - \operatorname{erf}\left(\frac{x_1}{\sqrt{2}\sigma_x}\right) \right) \frac{1}{2} \left(\operatorname{erf}\left(\frac{y_2}{\sqrt{2}\sigma_y}\right) - \operatorname{erf}\left(\frac{y_1}{\sqrt{2}\sigma_y}\right) \right). \end{aligned} \quad (34)$$

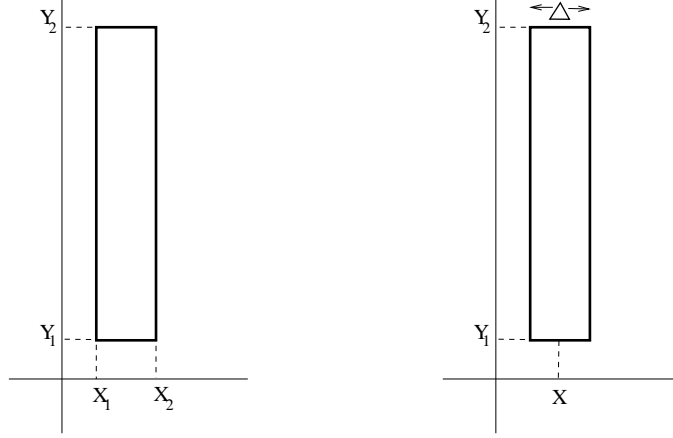


Figure 9: The integral of a Gaussian over a rectangle of sides parallel to the principal axes of the Gaussian factorizes, yielding the result (34).

If the Gaussian is isotropic, then all axes are principal and expression (34) holds. When the Gaussian is not isotropic (say $\sigma_y < \sigma_x$) we may dilate the y direction by a factor σ_x/σ_y to make it isotropic, as shown in Fig. 10 (this transformation is also used in [8]). A dilation, like a projection, is a linear transformation. Therefore, it transforms parallel lines into parallel lines. If the eigenaxes of the dilation are not parallel to the sides of the rectangle, the rectangle is transformed not into another rectangle but into a parallelogram. However, if the rectangle is very elongated we can again argue as in subsection 2.1.2 and suppose that it will transform into almost another rectangle. In particular, we suppose that the dilation of the rectangle can be well approximated by a rectangle whose long axis is the dilated axis and whose width is the dilated width. Since the new Gaussian is isotropic, its axes may be rotated arbitrarily and still be principal axes. We rotate them so as to render them parallel to the sides of the dilated rectangle, as shown in Fig. 10, and then formula (34) can be applied.

In order to adapt the result (34) to the approximation that we have described, we rewrite it as follows:

$$\frac{1}{2} \left(\operatorname{erf} \left(\frac{x' + \Delta'/2}{\sqrt{2}\sigma_x} \right) - \operatorname{erf} \left(\frac{x' - \Delta'/2}{\sqrt{2}\sigma_x} \right) \right) \frac{1}{2} \left(\operatorname{erf} \left(\frac{y'_2}{\sqrt{2}\sigma_y} \right) - \operatorname{erf} \left(\frac{y'_1}{\sqrt{2}\sigma_y} \right) \right), \quad (35)$$

where (x', y'_1) and (x', y'_2) are the coordinates of the end points of the dilated longitudinal axis of the tether in the new coordinates and Δ' is the width of the dilated rectangle. x', y'_1, y'_2 and Δ' are found in Appendix 2 by elementary geometry.

Substitution of these four quantities into formula (35) yields:

$$\frac{1}{2} \left(\operatorname{erf} \left(\frac{1}{\sqrt{2}} \frac{1}{\sigma_x \sigma_y} \frac{\sigma_y^2 x_2 (x_2 - x_1) + \sigma_x^2 y_2 (y_2 - y_1)}{\sqrt{\sigma_y^2 (x_2 - x_1)^2 + \sigma_x^2 (y_2 - y_1)^2}} \right) - \operatorname{erf} \left(\frac{1}{\sqrt{2}} \frac{1}{\sigma_x \sigma_y} \frac{\sigma_y^2 x_1 (x_2 - x_1) + \sigma_x^2 y_1 (y_2 - y_1)}{\sqrt{\sigma_y^2 (x_2 - x_1)^2 + \sigma_x^2 (y_2 - y_1)^2}} \right) \right)$$

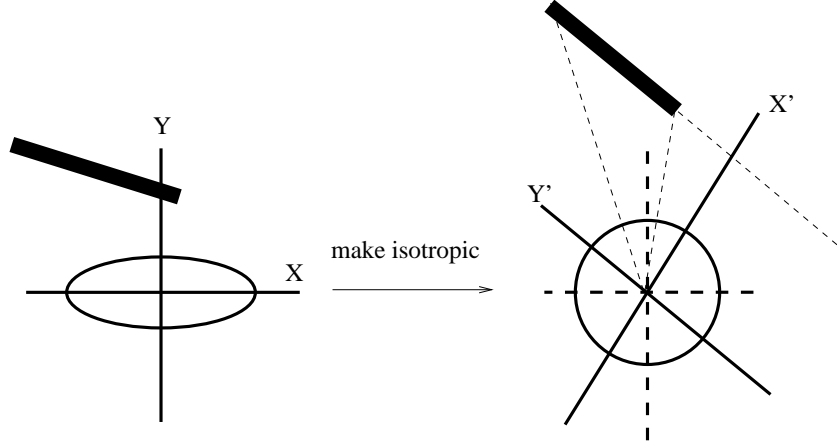


Figure 10: The transformation shown allows the use of the simple formula (34) for the computation of the Gaussian probability above any thin rectangle.

$$\frac{1}{2} \left(\operatorname{erf} \left(\frac{\sqrt{(x_2 - x_1)^2 + (y_2 - y_1)^2}}{\sqrt{2} \sqrt{\sigma_y^2 (x_2 - x_1)^2 + \sigma_x^2 (y_2 - y_1)^2}} \left(\frac{x_2 y_1 - x_1 y_2}{\sqrt{(x_2 - x_1)^2 + (y_2 - y_1)^2}} + \frac{\Delta}{2} \right) \right) - \operatorname{erf} \left(\frac{\sqrt{(x_2 - x_1)^2 + (y_2 - y_1)^2}}{\sqrt{2} \sqrt{\sigma_y^2 (x_2 - x_1)^2 + \sigma_x^2 (y_2 - y_1)^2}} \left(\frac{x_2 y_1 - x_1 y_2}{\sqrt{(x_2 - x_1)^2 + (y_2 - y_1)^2}} - \frac{\Delta}{2} \right) \right) \right). \quad (36)$$

The coordinates of the ends of the tether are good coordinates to derive the two preceding formulae, but are not as practical as the following five geometrical parameters: the b-plane coordinates (x and y) of the geometrical center of the rectangle, the rectangle length L and width Δ projected on the b-plane, and the orientation angle, Λ , of the longest rectangle axis with respect to the x eigenaxis of the covariance ellipsoid. In this way the coordinates of the four vertices of the rectangle in eq. (36) can be written as:

$$x_{1,2} = x \pm \frac{L}{2} \cos \Lambda; \quad y_{1,2} = y \pm \frac{L}{2} \sin \Lambda, \quad (37)$$

leading to:

$$\frac{1}{4} \left\{ \operatorname{erf} \left[\frac{D^2 L/2 + x \sigma_y^2 \cos \Lambda + y \sigma_x^2 \sin \Lambda}{\sqrt{2} D \sigma_x \sigma_y} \right] + \operatorname{erf} \left[\frac{D^2 L/2 - x \sigma_y^2 \cos \Lambda - y \sigma_x^2 \sin \Lambda}{\sqrt{2} D \sigma_x \sigma_y} \right] \right\} \left\{ \operatorname{erf} \left[\frac{\Delta/2 + |y \cos \Lambda - x \sin \Lambda|}{\sqrt{2} D} \right] + \operatorname{erf} \left[\frac{\Delta/2 - |y \cos \Lambda - x \sin \Lambda|}{\sqrt{2} D} \right] \right\}, \quad (38)$$

where:

$$D \equiv \sqrt{\sigma_x^2 \sin^2 \Lambda + \sigma_y^2 \cos^2 \Lambda}. \quad (39)$$

4.3 The disk

The projection of a circle of radius r which makes an angle α with the encounter plane is an ellipse of semiaxes $r \cos \alpha$ and r . The Minkowski sum of this ellipse with a circle of radius R is not another ellipse, but it is enclosed by an ellipse of semiaxes $r \cos \alpha + R$ and $r \frac{r \cos \alpha + R}{r \cos \alpha} = \frac{r \cos \alpha + R}{\cos \alpha}$, as shown in Fig. 11.

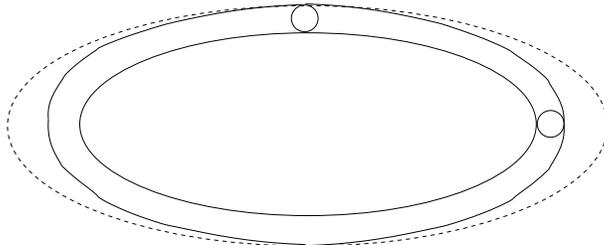


Figure 11: The Minkowski sum of an ellipse and a circle is enclosed by the ellipse shown.

In order to find the probability enclosed by this ellipse we dilate along the direction of the shorter axis by a factor $1/\cos \alpha$, so that the ellipse becomes a circle. If the direction of the shorter axis is \vec{w} , then the sigmas of the Gaussian have to be multiplied by the factors $(\vec{w} \cdot \vec{i})/\cos \alpha$ and $(\vec{w} \cdot \vec{j})/\cos \alpha$, respectively. We are then in a position to apply any of a number of algorithms devised in the last decades in the field of spatial debris to compute the Gaussian probability caught by a circle [2, 3, 4, 5, 6, 7].

5 Numerical study

In this section we are going to discuss the advantages of our formulae over the sphere approximation and present some numerical results.

There are two kinds of geometrical approximations. In the first kind the projection of the object is approximated by a circumscribing circle, in the second by a simpler geometrical figure of the same area. In both kinds the advantage of a geometrically exact treatment over an approximation depends of course on the shape of the object.

In this paragraph we discuss the first kind for the computation of a collision rate. If this kind of approximation is used to compute a probability of collision, then the error with respect to the integration of the Gaussian over the true projection can be even larger. For a tether and a plane figure the advantage is large. Debris can be large or small, but small debris is the most abundant. For small debris the Steiner-Minkowski formula (6) shows that only the area of the projection of the target matters. For a tether of length $2R$ and diameter d the area of its average projection is $\pi dR/2$, while the area of the projection of the circumscribing sphere is πR^2 . For a disk of radius R and its circumscribing sphere the average projected areas are, respectively, $\pi R^2/2$ and πR^2 . Thus for these two cases the ratios of the area of the average projection to the area of the projection of the circumscribing sphere are $d/(2R)$ (in reality less than 0.01) and $1/2$, respectively. For the International Space Station this ratio is between 0.01 and 0.1 (see Chapter 6 of [4]). Therefore exact geometrical formulae can significantly improve the

predictions obtained with the circumscribing sphere. When the debris is not small the Steiner-Minkowski formula (6) shows that the approximation by a circumscribing circle becomes better.

In this paragraph we discuss the second kind for the computation of a probability of collision first, then for the computation of a collision rate. We give two examples which have to do with sails and tethers, respectively. a) Isotropic Gaussian of $\sigma=10$ m centered at the origin. The probability over the square of vertices $(10,0),(20,0),(20,10),(10,10)$ m is 0.068, while the probability over the parallelogram of vertices $(15,0),(25,0),(15,10),(5,10)$ m, which has the same area and center, is 0.035. b) Isotropic Gaussian of $\sigma=20$ m centered at the origin. The probability over a rectangle of center at $(20,0)$ m, 2000 m long along the y direction and 2 cm long along the x direction is 0.00024, while the probability over an ellipse with the same center, area and aspect ratio as the rectangle is 0.00027. The difference is important in the first case and (given the uncertainty of the data) only marginally important in the second case. But performing calculations with the algorithm provided in subsection V.A of this article (see also <http://sdg.aero.upm.es/index.php/online-apps/gaussian-over-parallelogram>) is almost as fast for the parallelogram as for a rectangle. We have not compared the speeds of the algorithm for the parallelogram and the various algorithms for the disk, but we believe that the algorithm for the parallelogram is faster than any of them. When the projection of the object is approximated by a circle of the same area, the Steiner-Minkowski formula (6) shows that the approximation underestimates the collision rate (perhaps only by a small amount), because the circle is the figure of least perimeter for a given area.

To summarize, approximating a parallelogram by a simpler geometrical figure does not make the calculation faster.

The collision probability of a sail against debris is of the same order of magnitude (the ratio 1/2 mentioned at the beginning of this section) as the probability of collision of a round sail or even of a balloon of similar dimensions. The only case in which the collision probability would be significantly different is when the debris has a relative velocity which makes a small angle with the surface of the sail. In that case the projection of the sail would be a very elongated parallelogram, that is, a figure somewhat similar to a tether. Therefore we are going to limit the numerical exploration of the formulae to the case of a tether. Before doing that we note that when considering collisions with a sail, one has to distinguish between collision with the tissue of the sail only and collisions with the sail and its masts (also called booms) [26], but going into that is beyond the scope of this article.

Formula (38) depends on $x, y, \Lambda, \sigma_x, \sigma_y, L$ and Δ , which makes a thorough exploration of its parameter space an almost impossible task. We set $L = 2000$ m and present some results in two of the most representative situations, which are depicted in figures 12 and 13. It is argued in [7] that one of the sigmas should range between 4 and 4096 m, while the other should range between 4 and 256 m. Here we have made σ_x range between 2 and 2048 m and σ_y range between 2 and 128 m.

Perhaps the main question is: how close can the tether get to the spacecraft without danger? By danger we mean probability of collision greater than 10^{-3} or 10^{-4} . The distance corresponding to 10^{-5} is also shown because one might want to make an evasive maneuver so that the probability of collision with the tether diminishes from 10^{-3} or 10^{-4}

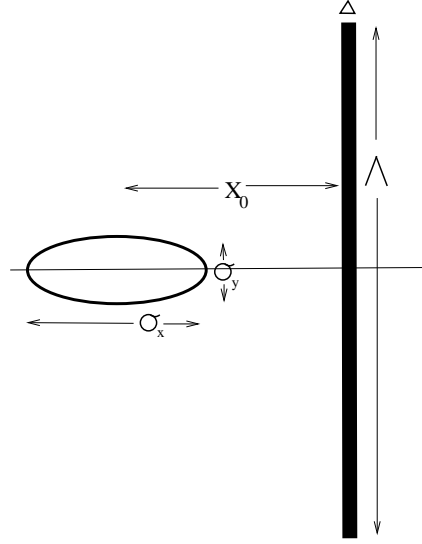


Figure 12: The dark rectangle stands for the Minkowski sum depicted in Fig. 1. The tether is at a distance $|x_0|$ from the origin.

to 10^{-4} or 10^{-5} .

The numbers that appear in the tables which follow are distances in meters. We have made the following choices of Δ . $\Delta = 0.07$ m because this corresponds (supposing that the width of the tether is 2 cm) to a sphere of 5 cm diameter which is the smallest detectable sphere by radar. $\Delta = 0.3$ m because this corresponds roughly to a sphere of 12 kg which is the largest sphere which breaks when colliding against a tether [26]. $\Delta = 2$ m and $\Delta = 8$ represent a medium and a large spacecraft, respectively.

$\Lambda = \pi/2$, $\Delta = 0.07$ m.

$\sigma_x \setminus p$	10^{-3}	10^{-4}	10^{-5}
2	4.6	6.3	7.6
8	12.6	21.3	27.4
32	0	66.6	95.7
128	0	160	318
512	0	0	943
2048	0	0	1613

$\Lambda = \pi/2$, $\Delta = 0.3$ m.

$\sigma_x \setminus p$	10^{-3}	10^{-4}	10^{-5}
2	5.72	7.16	8.34
8	18.6	25.3	30.6
32	52	86	110
128	0	271	386
512	0	667	1285
2048	0	0	3848

$\Lambda = \pi/2$, $\Delta = 2$ m.

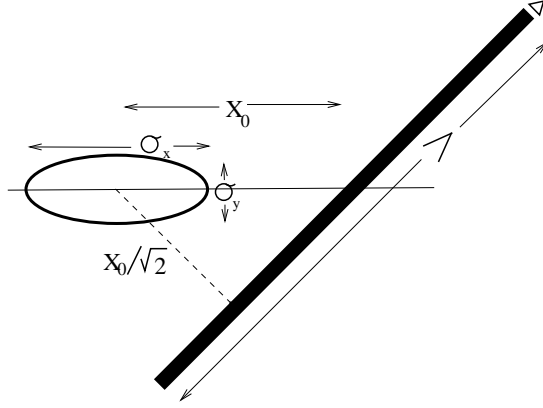


Figure 13: The dark rectangle stands for the Minkowski sum depicted in Fig. 1. The tether is at a distance $|x_0|/\sqrt{2}$ from the origin.

$\sigma_x \setminus p$	10^{-3}	10^{-4}	10^{-5}
2	7.16	8.43	9.52
8	24.3	29.8	34.4
32	81.2	106	127
128	245	368	459
512	482	1200	1627
2048	0	3378	5542

$$\Lambda = \pi/2, \Delta = 8 \text{ m.}$$

$\sigma_x \setminus p$	10^{-3}	10^{-4}	10^{-5}
2	10.2	11.4	12.6
8	29	34	38.1
32	97	119	138
128	325	425	506
512	482	1200	1837
2048	1929	4800	6508

The reader might find a little puzzling that for large σ_x and small Δ the closest allowed distance is sometimes 0. This means that no matter where the center of the tether is, the probability of collision is smaller than 10^{-3} . The first example of this shown in the tables is when $\Lambda = \pi/2$, $\Delta = 0.07$, $L = 2000$, $y = 0$, $\sigma_x = 128$. In Fig. 14 the probability of collision p versus the distance x is shown for the said values and one can see that $p < 10^{-3}$ everywhere.

In the first three examples the sequences for the distances when $p = 10^{-3}$ are 4.6, 12.6, 0; 5.72, 18.6, 52, 0 m and 7.16, 24.3, 81.2, 245, 482, 0 m. This may lead to the wrong conclusion that the value 0 is arrived at suddenly or discontinuously. This is not so, the apparent discontinuity comes from the fact that the values of the sigma are taken in geometric progression. To understand why the 0 is reached smoothly, think of a segment on the real line and think of what happens when you increase sigma starting from 0. As you increase sigma there is first a wave of probability which floods the segment. But after some sigma, the segment is inside the convex part of the Gaussian and the probability

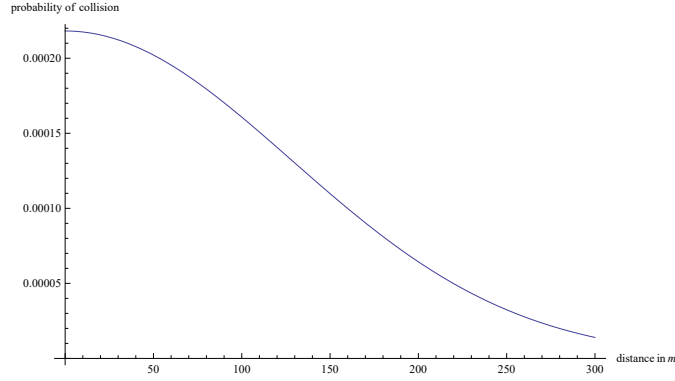


Figure 14: Irrespective of the relative position, $p < 10^{-3}$ is guaranteed.

caught in the segment begins to spread and thin out. If the segment is reduced to a point it is easy to see analytically that the Gaussian, as a function of σ , has a maximum at $\sigma = 1$, precisely the point where it changes from convex to concave. Thus, as sigma increases, the segment can be moved to the origin until it reaches 0.

$\Lambda = \pi/4$, $\Delta = 0.07$ m. Now the minimum distance depends on σ_y .

$\sigma_y = 2048$ m.

$\sigma_x \setminus p$	10^{-3}	10^{-4}
2	0	0
8	0	0
32	0	0
128	0	0

$\sigma_y = 512$ m.

$\sigma_x \setminus p$	10^{-3}	10^{-4}
2	0	0
8	0	0
32	0	0
128	0	0

$\sigma_y = 128$ m.

$\sigma_x \setminus p$	10^{-3}	10^{-4}	10^{-5}
2	0	136	237
8	0	136	237
32	0	138	243

$\sigma_y = 32$ m.

$\sigma_x \setminus p$	10^{-3}	10^{-4}	10^{-5}
2	15	51	70
8	14	52	72

$\sigma_y = 8$ m.

$\sigma_x \setminus p$	10^{-3}	10^{-4}	10^{-5}
2	10	16	20

$\Lambda = \pi/4$, $\Delta = 0.3$ m. Now the minimum distance depends on σ_y .

$\sigma_y = 2048$ m.

$\sigma_x \setminus p$	10^{-3}	10^{-4}
2	0	0
8	0	0
32	0	0
128	0	0

$\sigma_y = 512$ m.

$\sigma_x \setminus p$	10^{-3}	10^{-4}	10^{-5}
2	0	499	502
8	0	496	508
32	0	487	532
128	0	479	635

$\sigma_y = 128$ m.

$\sigma_x \setminus p$	10^{-3}	10^{-4}	10^{-5}
2	68	205	283
8	68	206	283
32	66	211	291

$\sigma_y = 32$ m.

$\sigma_x \setminus p$	10^{-3}	10^{-4}	10^{-5}
2	41	64	80
8	42	65	82

$\sigma_y = 8$ m.

$\sigma_x \setminus p$	10^{-3}	10^{-4}	10^{-5}
2	14	19	23

$\Lambda = \pi/4$, $\Delta = 2$ m. Now the minimum distance depends on σ_y .

$\sigma_y = 2048$ m.

$\sigma_x \setminus p$	10^{-3}	10^{-4}	10^{-5}
2	0	501	503
8	0	505	512
32	0	520	546
128	0	579	688

$\sigma_y = 512$ m.

$\sigma_x \setminus p$	10^{-3}	10^{-4}	10^{-5}
2	455	501	503
8	455	507	513
32	452	527	551
128	420	616	709

$\sigma_y = 128$ m.

$\sigma_x \setminus p$	10^{-3}	10^{-4}	10^{-5}
2	189	271	333
8	189	271	334
32	193	278	343

$\sigma_y = 32$ m.

$\sigma_x \setminus p$	10^{-3}	10^{-4}	10^{-5}
2	61	78	92
8	62	80	94

$\sigma_y = 8$ m.

$\sigma_x \setminus p$	10^{-3}	10^{-4}	10^{-5}
2	18	22	26

$\Lambda = \pi/4$, $\Delta = 8$ m. Now the minimum distance depends on σ_y .

$\sigma_y = 2048$ m.

$\sigma_x \setminus p$	10^{-3}	10^{-4}	10^{-5}
2	500	502	504
8	500	509	515
32	501	538	559
128	506	651	735

$\sigma_y = 512$ m.

$\sigma_x \setminus p$	10^{-3}	10^{-4}	10^{-5}
2	501	503	504
8	503	511	516
32	513	543	563
128	563	676	752

$\sigma_y = 128$ m.

$\sigma_x \setminus p$	10^{-3}	10^{-4}	10^{-5}
2	242	310	366
8	242	311	367
32	248	319	376

$\sigma_y = 32$ m.

$\sigma_x \setminus p$	10^{-3}	10^{-4}	10^{-5}
2	72	87	100
8	73	89	102

$\sigma_y = 8$ m.

$\sigma_x \setminus p$	10^{-3}	10^{-4}	10^{-5}
2	22	26	29

Generally speaking one decomposes an object into various geometrically simple objects and computes the collision probability for each of them. But it turns out that the contribution to the overall probability of collision of the end masses is almost always negligible compared to the contribution of the tether. The reason is that the perimeter of the tether, p_t , is about 1,000 longer than the perimeter of the any of the end masses, p_m . Their collision cross sections are about $2p_t r_s$ and $p_m r + \pi r_s^2 \ll 2p_t r_s$, where r_s is the radius of the sphere which might collide with the tether. Only when one of the sigmas is much smaller than the other (say, $\sigma_y = 4$ m and $\sigma_y = 500$ m) the end-mass lies on the x axis and the tether is perpendicular to the longest sigma, then both contributions are about the same. Otherwise the contribution of the tether is orders of magnitude larger.

The most dangerous angle Λ is when the tether is parallel to the eigenaxis of smallest sigma, because then all of the probability along that axis is caught.

The case $\Delta < 0.3$ m is a catastrophic collision, because pieces of debris are generated by the impact (not many pieces, since $\Delta < 0.3$ m). The case $\Delta > 0.3$ m is not catastrophic for the object meeting the tether but is still catastrophic for the tether, which gets cut in two.

In most of the situations an evasive maneuver of the order of a hundred meters suffices. When the sphere which might collide with the tether is small ($\Delta < 0.3$ m), there are many instances in which an evasive maneuver is not necessary because the collision probability is small even when the nominal trajectories collide. It seems that only when the angle Λ is unfavorable and the largest sigma is large, evasive maneuvers of the order of a few kilometers are necessary.

6 Conclusions

The formulae given in this article make it possible to improve the enveloping sphere or same area circle approximations for the computations of collision rates or probabilities when one of the objects is a circle, a rectangle or a very long rectangle or cylinder. This improvement is done without any additional computational cost, since the formulae are all analytical except for the case of the collision probability of a rectangle, for which a very fast algorithm, available as an app, is provided.

The most direct application is to sails and tethers, which motivated this work, but other applications are possible. In general one may decompose a complex aircraft in various pieces, and separately compute the probability of collision for each. When one of the pieces is a solar panel then the formulae for the rectangle can be used. Of course this leaves the problem of mutual shadowing, but this would be a topic for future work.

Appendix 1

The goal of this Appendix is to show the relation between the Minkowski sum and the probability that two objects, MM and SS , whose probability density functions (henceforth, pdf) of their positions are known, collide when the conditions of short-encounter model [2, 15, 3, 5, 4, 16, 1, 6] are fulfilled. In the short-encounter model this is equivalent to finding the probability that the projections M and S on the encounter plane overlap. The pdf's of the projections M and S on the encounter plane are the projections of the pdf's of MM and SS onto the encounter plane.

The Minkowski sum of two subsets \mathbf{M} and \mathbf{S} of a vector space is

$$\mathbf{M} \oplus \mathbf{S} \equiv \{\vec{m} + \vec{s} \text{ s. t. } \vec{m} \in \mathbf{M}, \vec{s} \in \mathbf{S}\}. \quad (36)$$

It follows from its definition that the Minkowski sum is commutative and associative.

The Minkowski sum of a set M and the set $\{\vec{t}\}$ consisting of just the vector \vec{t} is the translation of M by the vector \vec{t} . Thus $\mathbf{M} \oplus \mathbf{S}$ may be understood as the union of all translations of \mathbf{M} (or \mathbf{S}) by vectors in \mathbf{S} (or \mathbf{M}), that is:

$$\mathbf{M} \oplus \mathbf{S} = \bigcup_{\vec{t} \in \mathbf{S}} (\mathbf{M} \oplus \{\vec{t}\}) = \bigcup_{\vec{t} \in \mathbf{M}} (\{\vec{t}\} \oplus \mathbf{S}). \quad (37)$$

Since the Minkowski sum is commutative and associative,

$$(\{\vec{t}\} \oplus \mathbf{M}) \oplus \mathbf{S} = \{\vec{t}\} \oplus (\mathbf{M} \oplus \mathbf{S}).$$

The preceding formula tells us that the shape of the Minkowski sum of two subsets \mathbf{M} and \mathbf{S} of a vector space does not depend on their relative location.

Proposition. \mathbf{M} and \mathbf{S} overlap $\Leftrightarrow \vec{0} \in \mathbf{M} \oplus (-\mathbf{S}) \Leftrightarrow \vec{0} \in (-\mathbf{M}) \oplus \mathbf{S}$.

Proof:

\mathbf{M} and \mathbf{S} overlap $\Leftrightarrow \exists \vec{m}, \vec{s} | \vec{m} = \vec{s} \Leftrightarrow \exists \vec{m}, \vec{s} | \vec{m} - \vec{s} = \vec{0} \Leftrightarrow \vec{0} \in \mathbf{M} \oplus (-\mathbf{S}) \Leftrightarrow \vec{0} \in (-\mathbf{M}) \oplus \mathbf{S}$. **QED.**

This proposition is well known among the mathematicians who work with the Minkowski sum and can be found, for example, in the remark at the end of p. 12 of [17]. This proposition yields the condition for two bodies to overlap, thus there should be a connection between Minkowski sums and the forbidden region described in Fig. 1.

We note first that the sliding procedure described in Fig. 1 has to do with bodies which move in space, while the Minkowski sum has to do with subsets of a vector space. The

connection between both concepts is this: Let \mathbf{M} be a subset of R^2 (or R^3). Then the figure (or body) M is the class of subsets $M \equiv \{\{\vec{t}_M\} \oplus \mathbf{M}, \forall \vec{t}_M\}$. Likewise, $S \equiv \{\{\vec{t}_S\} \oplus \mathbf{S}, \forall \vec{t}_S\}$.

From the proposition this corollary follows: figures M and S overlap whenever \vec{t}_M and \vec{t}_S exist which satisfy

$$\vec{0} \in \mathbf{M} \oplus \{\vec{t}_M\} \oplus (-\mathbf{S}) \oplus \{-\vec{t}_S\} = \mathbf{M} \oplus (-\mathbf{S}) \oplus \{\vec{t}_M - \vec{t}_S\} \Leftrightarrow$$

$$\vec{t}_S - \vec{t}_M \in \mathbf{M} \oplus (-\mathbf{S}) \quad \text{or} \quad \vec{t}_M - \vec{t}_S \in (-\mathbf{M}) \oplus \mathbf{S}. \quad (38)$$

$\mathbf{M} \oplus (-\mathbf{S})$ is the set of translations which, when applied to the set \mathbf{S} , will make it overlap with \mathbf{M} . $(-\mathbf{M}) \oplus \mathbf{S}$ is the set of translations which, when applied to the set \mathbf{M} , will make it overlap with \mathbf{S} .

This corollary establishes the connection between the Minkowski sum and the determination of the region forbidden to a given point if collision is to be avoided. This is shown in Fig. 6.

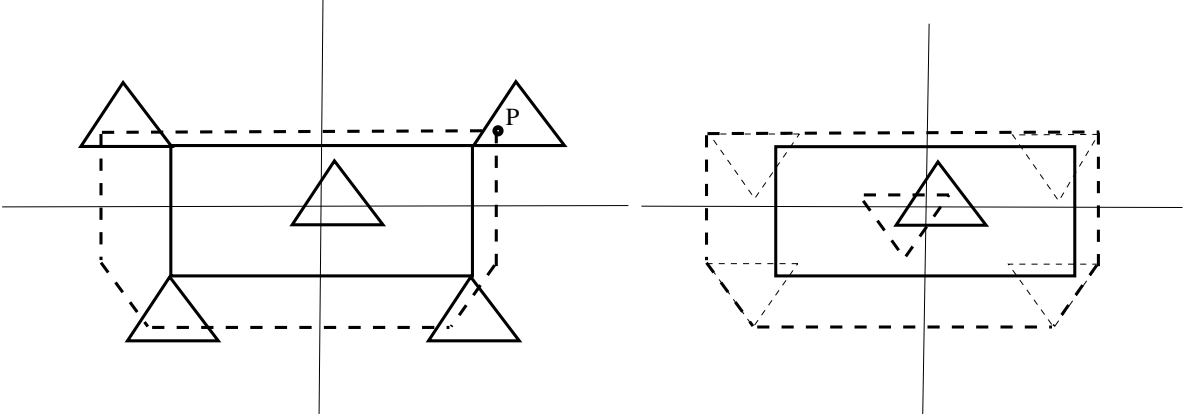


Figure 15: A is the rectangle and B is the triangle which contains the origin of coordinates. In the left figure the region forbidden to P is obtained by sliding the triangle around the rectangle, as in Fig. 1. In the right figure the triangle B is first inverted, then it is shown that the forbidden region is $A \oplus (-B)$. Note that the \vec{t}_B of the corollary is the position vector of the point P and \vec{t}_A of the corollary is $\vec{0}$, because the rectangle is not being moved.

Last we show the distributive property

$$\mathbf{A} \oplus (\mathbf{B} \cup \mathbf{C}) = (\mathbf{A} \oplus \mathbf{B}) \cup (\mathbf{A} \oplus \mathbf{C}), \quad (39)$$

which is used in subsection 3.2. It follows from the definition of Minkowski sum:

$$\mathbf{A} \oplus (\mathbf{B} \cup \mathbf{C}) = \{\vec{a} + \vec{d} \text{ s. t. } \vec{a} \in \mathbf{A} \wedge \vec{d} \in (\mathbf{B} \cup \mathbf{C})\} =$$

$$\{\vec{a} + \vec{d} \text{ s. t. } \vec{a} \in \mathbf{A} \wedge (\vec{d} \in \mathbf{B} \vee \vec{d} \in \mathbf{C})\}, \quad (40)$$

where \wedge is the logical “and” and \vee is the logical “or”. We continue:

$$\begin{aligned}
\mathbf{A} \oplus (\mathbf{B} \cup \mathbf{C}) &= \{\vec{a} + \vec{d} \text{ s. t. } (\vec{a} \in \mathbf{A} \wedge \vec{d} \in \mathbf{B}) \vee (\vec{a} \in \mathbf{A} \wedge \vec{d} \in \mathbf{C})\} = \\
&\{\vec{a} + \vec{d} \text{ s. t. } \vec{a} \in \mathbf{A} \wedge \vec{d} \in \mathbf{B}\} \cup \{\vec{a} + \vec{d} \text{ s. t. } \vec{a} \in \mathbf{A} \wedge \vec{d} \in \mathbf{C}\} = \\
&(\mathbf{A} \oplus \mathbf{B}) \cup (\mathbf{A} \oplus \mathbf{C}).
\end{aligned} \tag{41}$$

Appendix 2

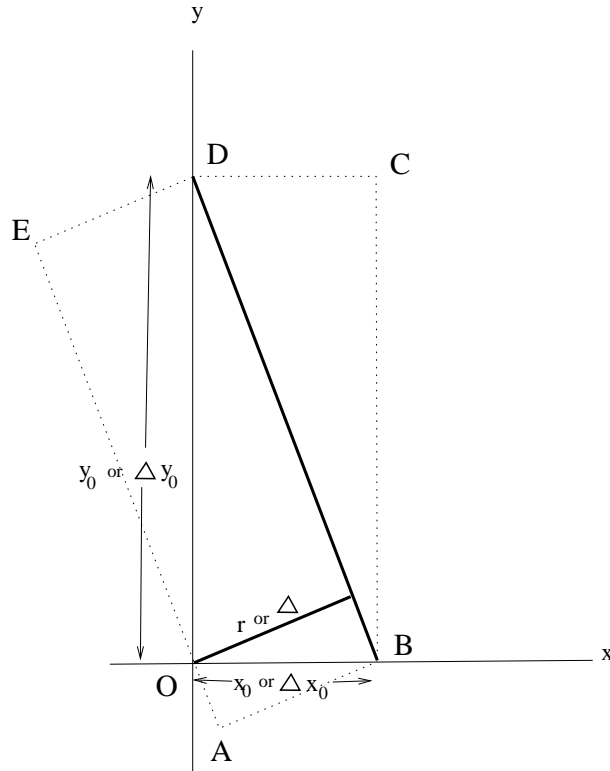


Figure 16: Rectangles EABD and OBCD have the same area, therefore $r\sqrt{x_0^2 + y_0^2} = x_0y_0$ or $\Delta\sqrt{\Delta x_0^2 + \Delta y_0^2} = \Delta x_0\Delta y_0$.

In this derivation we specify the straight lines by the coordinates of their extremes: $\vec{r}_1 = (x_1, y_1)$ and $\vec{r}_2 = (x_2, y_2)$. Let x_0 and y_0 be the x and y intercepts, respectively, of the straight line which is the longitudinal axis of the tether and let Δ be the distance between the parallel lines. The distance of the longitudinal axis of the tether to the origin, as shown in Fig. 16 is

$$\text{dist}(x_0, y_0) = \frac{|x_0y_0|}{\sqrt{x_0^2 + y_0^2}}. \tag{42}$$

Let σ_x and σ_y be the standard deviations of the Gaussian along its principal axes. After the dilation $y \rightarrow \frac{\sigma_x}{\sigma_y}y$ has taken place to make the Gaussian isotropic, the extremes of the new straight line are

$$\text{iso}(\vec{r}_i) = \left(x_i, \frac{\sigma_x}{\sigma_y}y_i \right) = \frac{1}{\sigma_y}(\sigma_y x_i, \sigma_x y_i). \quad (43)$$

The x and y intercepts of a straight line determined by its end points $\vec{r}_1 = (x_1, y_1)$ and $\vec{r}_2 = (x_2, y_2)$ are

$$\left. \begin{aligned} x_0(\vec{r}_1, \vec{r}_2) &= \frac{x_1 y_2 - y_1 x_2}{y_2 - y_1} \\ y_0(\vec{r}_1, \vec{r}_2) &= \frac{y_1 x_2 - x_1 y_2}{x_2 - x_1} \end{aligned} \right\}. \quad (44)$$

Then the distance of the new longitudinal axis to the origin is the x' that is needed in formula (35):

$$x' = \text{dist}(x_0(\text{iso}(\vec{r}_1), \text{iso}(\vec{r}_2)), y_0(\text{iso}(\vec{r}_1), \text{iso}(\vec{r}_2))) = \frac{\sigma_x |x_1 y_2 - y_1 x_2|}{\sqrt{\sigma_y^2 (x_2 - x_1)^2 + \sigma_x^2 (y_2 - y_1)^2}}. \quad (45)$$

The factor by which the distance to the origin has changed after the dilation is

$$\begin{aligned} & \frac{\sigma_x |x_1 y_2 - y_1 x_2|}{\sqrt{\sigma_y^2 (x_2 - x_1)^2 + \sigma_x^2 (y_2 - y_1)^2}} \frac{\sqrt{(x_2 - x_1)^2 + (y_2 - y_1)^2}}{|x_1 y_2 - y_1 x_2|} = \\ & \frac{\sqrt{(x_2 - x_1)^2 + (y_2 - y_1)^2}}{\sqrt{\sigma_y^2 (x_2 - x_1)^2 + \sigma_x^2 (y_2 - y_1)^2}} \sigma_x. \end{aligned} \quad (46)$$

This is also the factor by which the width changes after the dilation, therefore the Δ' that is needed in formula (35) is:

$$\Delta' = \frac{\sqrt{(x_2 - x_1)^2 + (y_2 - y_1)^2}}{\sqrt{\sigma_y^2 (x_2 - x_1)^2 + \sigma_x^2 (y_2 - y_1)^2}} \sigma_x \Delta. \quad (47)$$

The unit vector which points from $\text{iso}(\vec{r}_1)$ to $\text{iso}(\vec{r}_2)$ is

$$\vec{u} = \frac{(\sigma_y(x_2 - x_1), \sigma_x(y_2 - y_1))}{\sqrt{\sigma_y^2 (x_2 - x_1)^2 + \sigma_x^2 (y_2 - y_1)^2}}.$$

Then the coordinates y'_1 and y'_2 that are needed in formula (35) are:

$$y'_i = \text{iso}(\vec{r}_i) \cdot \vec{u}, \quad i = 1, 2. \quad (48)$$

Appendix 3

Let us consider the following bivariate normal (BVN) probability:

$$L(h, b, \rho) = \frac{1}{2\pi\sqrt{1-\rho^2}} \int_h^\infty \int_k^\infty \exp \frac{-(x^2 - 2\rho xy + y^2)}{2(1-\rho^2)} dx dy \quad (49)$$

related to the standard BVN distribution by the expression $\Phi((x_0, y_0), \rho) = L(-x_0, -y_0, \rho)$. Although it would be possible to evaluate eq. (49) directly using a 2D numerical integration method, a faster algorithm can be achieved by reducing the problem to a single integral. Following previous work by Drezner and Wesolowski [27], Genz proposes in [25] to apply the formula for the partial derivative of the BVN distribution with respect to the correlation derived by Plackett [28]:

$$\frac{\partial L(h, k, r)}{\partial r} = \frac{1}{2\pi\sqrt{1-r^2}} \exp \frac{-(h^2 - 2rhk + k^2)}{2(1-r^2)}, \quad (50)$$

and integrate it in r to obtain an expression for L in terms of a single integral in the correlation.

The most straightforward choice would be to integrate between 0 and ρ , since the initial value for L at $r = 0$ is easily computed as the product of two univariate normal distributions. However, the singularity at $|r| = 1$ negatively affects the accuracy of the numerical integration for cases with $|\rho| \sim 1$. To alleviate this issue Drezner and Wesolowsky [27] proposed to instead integrate between ρ and $\text{sign}(\rho)$: integrating only over the small region close to the singularity improves the numerical behavior, and the value of L at $r = \pm 1$ can also be expressed in terms of univariate normal distributions. Unfortunately, this new integral can still present numerical problems for h close but not equal to $\text{sign}(\rho)k$. Drezner and Wesolowsky circumvented this by applying a clever trick: they expanded part of the integrand in Taylor series of $\sqrt{1-r^2}$, providing the analytic integral of the polynomial part and performing the numerical integral of the remainder. The original work by Drezner and Wesolowsky [27] uses the Taylor expansion up to order 3, and Genz [25] later extended the result to order 5.

Building upon all these developments, Genz [25] defines an efficient algorithm for the numerical evaluation of L in double precision. On the one hand, he uses the integral between 0 and ρ for $|\rho| \leq 0.925$, and the modified integral between ρ and $\text{sign}(\rho)$ for $|\rho| > 0.925$. To improve the numerical treatment of the integrands, he does the changes of variable $r = \sin(\theta)$ and $x = \sqrt{1-r^2}$, respectively. On the other hand, he applies Gauss-Legendre integration rules with enough points to maintain an absolute error less than $5 \cdot 10^{-16}$ (following extensive numerical tests, he proposes the 6 points rule for $|\rho| < 0.3$, the 12 points rule for $0.3 \leq |\rho| < 0.75$, and the 20 points rule for $|\rho| > 0.75$).

This work uses an in-house implementation of the original Genz algorithm, modified in order to deal with the more general problem of integrating the Gaussian over a parallelogram, as detailed in subsection 4.1.

Funding Sources

This work has been supported by the ESA Contract No. 4000119560/17/F/MOS ('Environmental aspects of passive de-orbiting devices'). This work has been supported by the

Spanish Ministry of Economy and Competitiveness within the framework of the research project ESP2017-87271-P.

Acknowledgments

We thank María de los Angeles Hernández Cifre and Hodei Urrutxua Cereijo for remarks and references.

References

- [1] Claudio Bombardelli and Javier Hernando-Ayuso. Optimal impulsive collision avoidance in low earth orbit. *Journal of Guidance, Control, and Dynamics*, 38(2):217–225, 2015. doi: 10.2514/1.G000742.
- [2] J. L. Foster and H. S. Estes. A parametric analysis of orbital debris collision probability and maneuver rate for space vehicles. *NASA/JSC-25898*, 1992.
- [3] Russell P. Patera. General method for calculating satellite collision probability. *Journal of Guidance, Control, and Dynamics*, 24(4):716–722, 2001. doi: 10.2514/2.4771.
- [4] F. Kenneth Chan. *Spacecraft Collision Probability*. American Institute of Aeronautics and Astronautics, 2008. ISBN-13: 978-1884989186, doi: 10.2514/4.989186.
- [5] Salvatore Alfano. A numerical implementation of spherical object collision probability. *Journal of the Astronautical Sciences*, 53(1):103–109, 2005.
- [6] Romain Serra, Denis Arzelier, Mioara Joldes, Jean-Bernard Lasserre, Aude Rondepierre, and Bruno Salvy. Fast and accurate computation of orbital collision probability for short-term encounters. *Journal of Guidance, Control and Dynamics*, 39(5):1009–1021, 2016. doi: 10.2514/1.G001353.
- [7] Ricardo García-Pelayo and Javier Hernando-Ayuso. Series for collision probability in short-encounter model. *Journal of Guidance, Control, and Dynamics*, 39(8):1908–1916, 2016. doi: 10.2514/1.G001754.
- [8] Yuchen Xie and Ken Chan. Collision probability for rectangular cross sections. In *2018 Space Flight Mechanics Meeting, AIAA SciTech Forum, (AIAA 2018-2231)*, 2018. doi: 10.2514/6.2018-2231.
- [9] S. Alfano. Volumetric Encounter Analysis Enhancements. *AAS/AIAA Astrodynamics Specialist Conference, Vail, CO, August 10-13*, 2015.
- [10] Jer-Chyi Liou et al. The new nasa orbital debris engineering model ordem2000. Technical report, National Aeronautics and Space Administration, Johnson Space Center, 2002.

- [11] S Flegel, J Gelhaus, C Wiedemann, P Vorsmann, M Oswald, S Stabroth, H Klinkrad, and H Krag. The master-2009 space debris environment model. In *Fifth European Conference on Space Debris*, volume 672, 2009.
- [12] Iso standard. *ISO 27852*, 2016.
- [13] S. Alfano. Accomodating Rectangular Objects in Probability Calculations. *AAS/AIAA Astrodynamics Specialist Conference, Paper No. AIAA 2004-5217*, 2004.
- [14] S. Alfano. Method for determining maximum conjunction probability of rectangular-shaped objects. (US 7,383,153 B2), 2008.
- [15] Maruthi R. Akella and Kyle T. Alfriend. Probability of collision between space objects. *Journal of Guidance, Control, and Dynamics*, 23(5):769–772, 2000. doi: 10.2514/2.4611.
- [16] Vincent T. Coppola. Including velocity uncertainty in the probability of collision between space objects. In *AAS/AIAA Spaceflight Mechanics Meeting*, volume AAS 12-247, 2012.
- [17] Rolf Schneider. *Convex Bodies: The Brunn-Minkowski Theory*. Cambridge University Press, 2nd expanded edition edition, 2014. ISBN: 9780521352208.
- [18] S. Alfano. Eliminating Assumptions Regarding Satellite Conjunction Analysis. *AAS Journal of the Astronautical Sciences*, 59(4):676–705, 2012. DOI: 10.1007/s40295-014-0002-4.
- [19] F. Kenneth Chan. Is the Probability of Collision of a Spacecraft Traversing Through the Earth’s Debris Environment Described by a Poisson Distribution? *27th Space Flight Mechanics Meeting*, AAS 17-244:1–16, 2017.
- [20] P. A. P. Moran. *An introduction to probability theory*. Clarendon Press, Oxford, 1968.
- [21] H. Klinkrad, P. Wegener, C. Wiedemann, J. Bendisch, and H. Krag. *Space Debris: Models and Risk Analysis, Chapter 3: Modeling of the Current Space Debris Environment*. Springer, 2006. ISBN: 3-540-25448-X.
- [22] Chuan Chih Hsiung. *A first course in differential geometry*. John Wiley & Sons, 1981. ISBN: 0-471-07953-7.
- [23] Manuel Castellet and Irene Llerena. *Álgebra lineal y geometría*. Reverté©, 1992. ISBN: 978-8429150094.
- [24] AP Alpatov, VV Beletsky, VI Dranovskii, VS Khoroshilov, AV Pirozhenko, Hans Troger, and AE Zakrzhevskii. *Dynamics of Tethered Space Systems*. CRC Press, 2010. ISBN: 978-1-4398-3685-9.

- [25] Alan Genz. Numerical computation of rectangular bivariate and trivariate normal and t probabilities. *Statistics and Computing*, 14(3):251–260, 2004. doi: 10.1023/B:STCO.0000035304.20635.31.
- [26] A. Francesconi, C. Giacomuzzo and B. Shaker Khan. Collision consequences for passive de-orbit devices. *ESA/ESOC Contract No. 4000119560/17/F/MOS. Environmental aspects of passive de-orbiting devices*, Technical Note 2, Version 2.0, 2017.
- [27] Zvi Drezner and George O Wesolowsky. On the computation of the bivariate normal integral. *Journal of Statistical Computation and Simulation*, 35(1-2):101–107, 1990. doi: 10.1080/00949659008811236.
- [28] Robin L Plackett. A reduction formula for normal multivariate integrals. *Biometrika*, 41(3/4):351–360, 1954. doi: 10.2307/2332716.